Electrical property mapping using MRI: analytical methods and implementations

Leijsen, R.L.

3

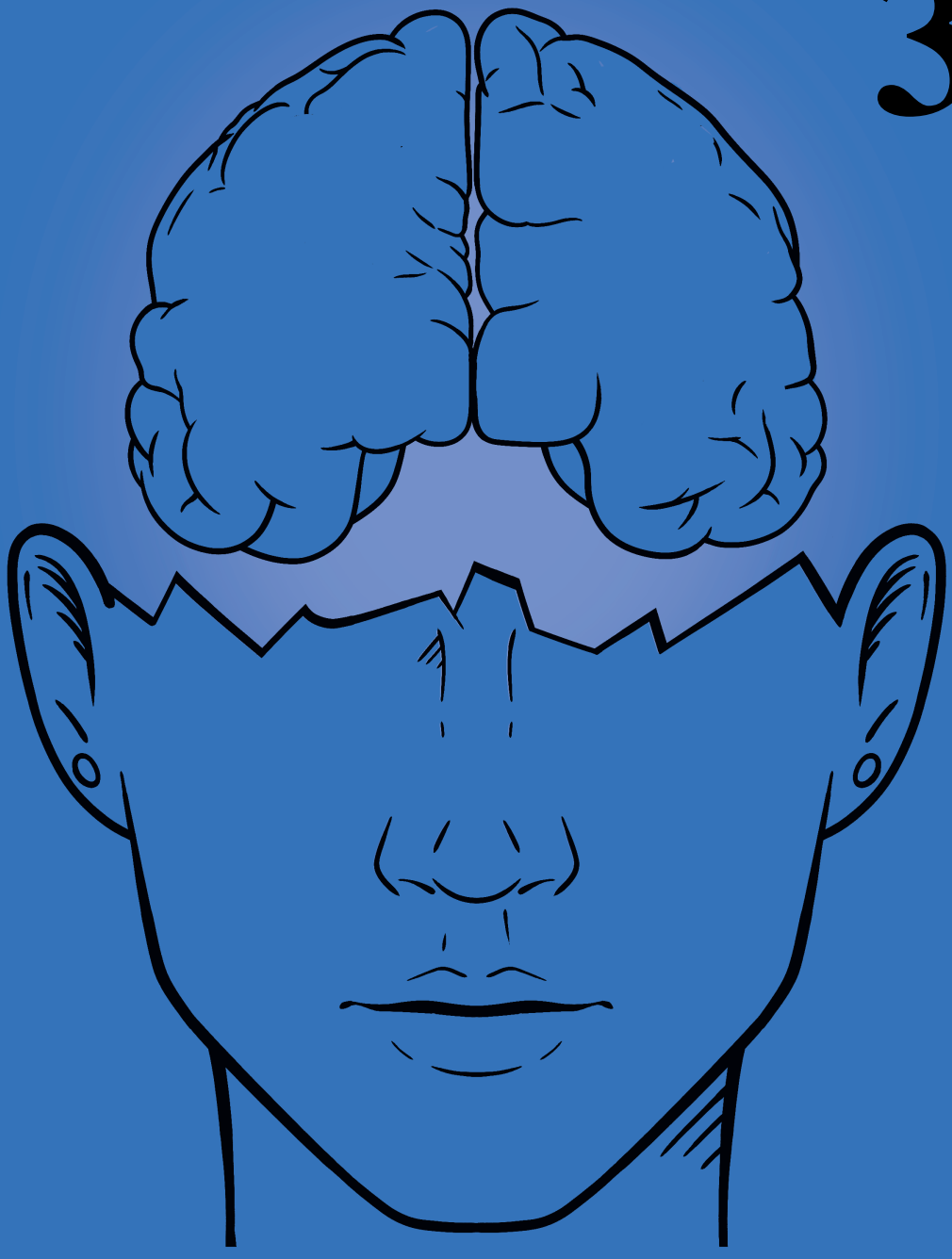

Developments in Electrical-Property Tomography Based on the Contrast-Source Inversion Method

Reijer L. Leijsen†, Patrick S. Fuchs†, Wyger M. Brink, Andrew G. Webb, and Rob F. Remis

This chapter appeared in Journal of Imaging, Vol. 5, no. 2, 25,
January 2019, DOI:10.3390/jimaging5020025

ABSTRACT

THE main objective of electrical properties tomography (EPT) is to retrieve the dielectric tissue parameters from B_1^+ data as measured by a magnetic resonance (MR) scanner. This is a so-called hybrid inverse problem in which the data is defined *inside* the reconstruction domain of interest. In this paper, we discuss recent and new developments in EPT based on the contrast source inversion (CSI) method. After a short review of the basics of this method, two- and three-dimensional implementations of CSI-EPT are presented along with a very efficient variant of 2D CSI-EPT called first-order induced current EPT (foIC-EPT). Practical implementation issues that arise when applying the method to measured data are addressed as well, and the limitations of a two-dimensional approach are extensively discussed. Tissue parameter reconstructions of an anatomically correct male head model illustrate the performance of two- and three-dimensional CSI-EPT. We show that a 2D implementation produces reliable reconstructions under very special circumstances only while accurate reconstructions can be obtained with 3D CSI-EPT.

3.1. INTRODUCTION

THE conductivity and permittivity values of different tissue types are of great importance in a variety of medical applications. In magnetic resonance (MR) safety [1] and hyperthermia treatment planning [2], for example, the conductivity tissue profiles are required to determine the specific absorption rate (SAR). The conductivity may also serve as a bio-marker in oncology or in acute stroke imaging [3]. The permittivity is important since it affects the spatial distribution of the transmitted electromagnetic field responsible for spin excitation.

Typically, the conductivity and permittivity values of tissue are measured *ex vivo* for a particular range of frequencies [4]. Other methods require elaborate hardware such as electrical impedance tomography (EIT) [5] or microwave imaging methods [6]. The objective of electrical properties tomography (EPT) is to retrieve these dielectric tissue values *in vivo* using an MR scanner and standard measurement protocols [3, 7]. Specifically, with an MR scanner, the so-called B_1^+-field, defined as $B_1^+ = (B_x + \mathrm{j}B_y)/2$, can be measured at a particular frequency of operation called the Larmor frequency. This frequency is proportional to the magnitude of the static background field B_0 via the relation $f = \gamma B_0$, where $\gamma = 42.577$ MHz T^{-1} is the proton gyromagnetic ratio divided by 2π, leading to MR operating frequencies of 128 MHz and 298 MHz for a 3 T and 7 T scanner, respectively.

Reconstruction of the dielectric tissue parameters is based on the measured B_1^+-field and what sets EPT apart from other more common inversion and imaging problems is that the measured B_1^+-field has its support *inside* the reconstruction domain. The EPT reconstruction problem therefore belongs to the class of so-called hybrid inverse problems [8] and several EPT techniques have been proposed to reconstruct the conductivity and permittivity profiles based on this internal B_1^+ data. Loosely speaking, these techniques can be divided into local differential-based approaches (see e.g. [9–12]) and global integral-based approaches (see e.g. [13–18]). Combinations of local and global methods have been developed as well [19, 20].

In this paper, we focus on a global integral-based EPT reconstruction method, called CSI-EPT, where a contrast source inversion (CSI) approach [21–23] is taken to solve the EPT reconstruction problem. In particular, in CSI-EPT the reconstruction problem is formulated as an optimization problem in which an objective function is iteratively minimized. This objective function consists of a term that measures the mismatch between modeled and measured data (data mismatch) and a term that measures the discrepancy in satisfying Maxwell's equations within the reconstruction domain using a global integral field representation (consistency mismatch). Including the second consistency term in the objective function is crucial to the performance of CSI as shown in [24].

Minimization of the objective function is carried out by iteratively updating a contrast function, which describes the dielectric constitution of the body part of interest, and a so-called contrast source, which is the product of the contrast function and the electric field strength. Updating takes place by fixing one variable and updating the other. More precisely, first the contrast function is fixed and the contrast source is updated and subsequently the contrast source is fixed and the contrast function is updated.

The CSI-EPT method was originally introduced in [14], where it was shown that

CSI-EPT is able to reconstruct strongly inhomogeneous conductivity and permittivity profiles within the center slice of an object placed in the center of a body coil in a 3 T MR scanner. The method was initially implemented for E-polarized electromagnetic fields in two-dimensional (2D) configurations in which the electric field is parallel to the bore axis (z-axis) and the magnetic field is purely transverse, because it is significantly less complex than a full three-dimensional implementation. The use of a 2D approach was justified, since it was shown that the electromagnetic field in the midplane of a birdcage coil essentially has an E-polarized field structure [25]. An efficient alternative to CSI-EPT, called first-order Induced Current EPT or foIC-EPT, has been presented as well in [20]. This method exploits the structure of the two-dimensional E-polarized field to efficiently reconstruct the tissue profiles in the midplane of the transmit coil. The foIC-EPT method is significantly faster than CSI-EPT and produces reconstructions in real time with essentially the same quality as 2D CSI-EPT.

The CSI-EPT method has recently been extended to three-dimensional (3D) configurations in [26]. With this 3D implementation of CSI-EPT, volumetric conductivity and permittivity profiles are obtained, and it is no longer necessary to restrict the reconstruction domain to the midplane of a transmit coil. Moreover, 3D CSI-EPT is based on the vectorial 3D Maxwell equations and no (E-polarized) field structure is assumed to be present as is the case in a 2D approach. Unfortunately, computation times dramatically increase compared with 2D CSI-EPT and foIC-EPT and, depending on the configuration, it may take 3D CSI-EPT hours or even days to converge even on dedicated high-performance computers or servers. Apart from possible preconditioning techniques that may be applied to accelerate the convergence of 3D CSI-EPT, 2D CSI-EPT or foIC-EPT may be preferable in practice, since reconstruction times are significantly shorter compared with 3D approaches.

In this paper, we thoroughly investigate this issue and compare reconstructions obtained with 2D CSI-EPT, foIC-EPT, and 3D CSI-EPT. Reconstruction artifacts in the conductivity and permittivity profiles, the modeled B_1^+-field, and the internal electric field are carefully studied. Our analysis shows that only under very special conditions is a 2D approach justified. Even if the electromagnetic field has an E-polarized field structure in the midplane of the transmit coil, imposing a two-dimensional field structure is generally too limiting an approximation unless the body part of interest and transmit coil strictly satisfy the longitudinal invariance condition.

This paper is organized as follows. In Section 3.2, the 2D and 3D CSI-EPT method is briefly reviewed and the governing integral representations are presented as well. A variant of 2D CSI-EPT, called foIC-EPT, is also presented and a detailed analysis of the performance of all three reconstruction methods is presented in Section 3.3 using a realistic head model from the Virtual Family [27]. A discussion with conclusions can be found in Section 3.4. Finally, we note that the position vectors in 2D and 3D are denoted by $\boldsymbol{\rho}$ and $\boldsymbol{x}$, respectively, and we use an $\exp(+\mathrm{j}\omega t)$ time convention.

3.2. THEORY

As mentioned above, the CSI-EPT algorithm operates on two unknowns and is based on two fundamental equations. Specifically, the unknowns in CSI-EPT are the contrast function χ and the contrast source $\boldsymbol{w}$ and the fundamental equations are the data

equation and object or state equation.

The contrast function describes the dielectric contrast of the body with respect to free space and is given by $\chi(\boldsymbol{x}) = \varepsilon_{\mathrm{r}}(\boldsymbol{x}) - 1 - \mathrm{j}\sigma(\boldsymbol{x})/\omega\varepsilon_0$, where $\varepsilon_{\mathrm{r}}(\boldsymbol{x})$ and $\sigma(\boldsymbol{x})$ are, respectively, the unknown relative permittivity and conductivity profiles of the body, ε_0 is the permittivity of free space, and ω is the Larmor frequency of operation. The contrast function has the bounded domain $\mathbb{D}$ that is occupied by the body as its support, that is the contrast function vanishes for $\boldsymbol{x} \notin \mathbb{D}$. Finally, we note that the contrast function is dimensionless and that its real part is determined by the permittivity profile, while its imaginary part is determined by the body's conductivity profile.

The contrast source in CSI-EPT is defined as $\boldsymbol{w} = \chi \boldsymbol{E}$, where $\boldsymbol{E}(\boldsymbol{x})$ is the electric field strength. Note that it is common to refer to $\boldsymbol{w}$ as a contrast source even though it is expressed in volt per meter and is actually a scaled electric field strength. The electric field strength is obviously also unknown, since the dielectric constitution of the body is unknown. Even though this field is not of primary interest in EPT, CSI-EPT does provide electric field reconstructions that may be used to reconstruct the local time-averaged power density that is dissipated into heat [1].

To arrive at the two fundamental equations of CSI-EPT, we set up a scattering formalism in which we make use of the linearity of Maxwell's equations and exploit the fact that the body occupies a bounded domain $\mathbb{D}$. In particular, we first determine the electromagnetic field that is present inside an empty birdcage coil. In practice, this so-called background field is computed using electromagnetic simulation software and we denote it by $\{\boldsymbol{E}^{\mathrm{bkg}}, \boldsymbol{B}^{\mathrm{bkg}}\}$. We note that here the assumption is made that the external currents are impressed and field independent. Consequently, antenna loading is not directly taken into account. The total electromagnetic field in presence of the body is denoted by $\{\boldsymbol{E}, \boldsymbol{B}\}$ and using the linearity of Maxwell's equations this field can be written as

$$\{\boldsymbol{E}, \boldsymbol{B}\} = \left\{\boldsymbol{E}^{\mathrm{bkg}}, \boldsymbol{B}^{\mathrm{bkg}}\right\} + \left\{\boldsymbol{E}^{\mathrm{sca}}, \boldsymbol{B}^{\mathrm{sca}}\right\}, \tag{3.1}$$

where $\{\boldsymbol{E}^{\mathrm{sca}}, \boldsymbol{B}^{\mathrm{sca}}\}$ is the scattered electromagnetic field due to the presence of the body. For this field we have the integral representations

$$\boldsymbol{B}^{\mathrm{sca}}(\boldsymbol{x}) = \int_{\boldsymbol{x}' \in \mathbb{D}} \underline{\boldsymbol{G}}^{\mathrm{BJ}}(\boldsymbol{x}, \boldsymbol{x}') \cdot \boldsymbol{w}(\boldsymbol{x}') \, \mathrm{d}V \quad \text{and} \quad \boldsymbol{E}^{\mathrm{sca}}(\boldsymbol{x}) = \int_{\boldsymbol{x}' \in \mathbb{D}} \underline{\boldsymbol{G}}^{\mathrm{EJ}}(\boldsymbol{x}, \boldsymbol{x}') \cdot \boldsymbol{w}(\boldsymbol{x}') \, \mathrm{d}V, \tag{3.2}$$

where $\underline{\boldsymbol{G}}^{\mathrm{EJ}}$ and $\underline{\boldsymbol{G}}^{\mathrm{BJ}}$ are essentially the electric-current to electric field and electric-current to magnetic field Green's tensors of the background medium. Note that these are the Green's tensors of a homogeneous background medium and the presence of the coil is not taken into account. Explicit expressions for these tensors are given below.

Having these integral representations at our disposal, we can now present the basic CSI-EPT equations. We start with the equation that relates the measured B_1^+-field to the contrast source. In particular, using the integral representation for the scattered magnetic field of Crefeq:intrep, we have

$$B_1^{+;\mathrm{sca}}(\boldsymbol{x}) = \frac{B_x^{\mathrm{sca}} + \mathrm{j}B_y^{\mathrm{sca}}}{2} = \frac{1}{2} \int_{\boldsymbol{x}' \in \mathbb{D}} \sum_{k=x,y,z} \left[G_{xk}^{\mathrm{BJ}}(\boldsymbol{x}, \boldsymbol{x}') + \mathrm{j} G_{yk}^{\mathrm{BJ}}(\boldsymbol{x}, \boldsymbol{x}') \right] w_k(\boldsymbol{x}') \, \mathrm{d}V, \tag{3.3}$$

which can be written more compactly as

$$B_1^{+;\mathrm{sca}}(\boldsymbol{x}) = \mathcal{G}_{\mathrm{dat}}\{\boldsymbol{w}\}(\boldsymbol{x}) \quad \text{for } \boldsymbol{x} \in \mathbb{D}, \tag{3.4}$$

where the linear data operator $\mathcal{G}_{\mathrm{dat}}$ is implicitly defined in Equation (3.3). Equation (3.4) is known as the *data equation* and relates the unknown contrast source $\boldsymbol{w}$ to the scattered B_1^+-field. Note that this scattered field is known, since $B_1^{+;\mathrm{sca}}(\boldsymbol{x}) = B_1^+(\boldsymbol{x}) - B_1^{+;\mathrm{bkg}}(\boldsymbol{x})$ and the total B_1^+-field is known through measurements, while the background field $B_1^{+;\mathrm{bkg}}(\boldsymbol{x})$ is known through simulations. The real phase is generally not known in practice, and the transceive phase approximation is often used, which can lead to reconstruction artefacts at higher frequencies [28].

The second basic CSI-EPT equation, called the *object* or *state equation*, is obtained from the integral representation for the scattered electric field as given by the second equation of Equation (3.2). Using the definition of the scattered electric field $\boldsymbol{E}^{\mathrm{sca}} = \boldsymbol{E} - \boldsymbol{E}^{\mathrm{bkg}}$, this integral representation can be written as

$$\boldsymbol{E}(\boldsymbol{x}) - \int_{\boldsymbol{x}' \in \mathbb{D}} \underline{\boldsymbol{G}}^{\mathrm{EJ}}(\boldsymbol{x}, \boldsymbol{x}') \cdot \boldsymbol{w}(\boldsymbol{x}')\, \mathrm{d}V = \boldsymbol{E}^{\mathrm{bkg}}(\boldsymbol{x}) \tag{3.5}$$

and multiplying the above equation by the contrast function χ we arrive at

$$\boldsymbol{w}(\boldsymbol{x}) - \chi(\boldsymbol{x}) \int_{\boldsymbol{x}' \in \mathbb{D}} \underline{\boldsymbol{G}}^{\mathrm{EJ}}(\boldsymbol{x}, \boldsymbol{x}') \cdot \boldsymbol{w}(\boldsymbol{x}')\, \mathrm{d}V = \chi(\boldsymbol{x}) \boldsymbol{E}^{\mathrm{bkg}}(\boldsymbol{x}) \quad \text{for } \boldsymbol{x} \in \mathbb{D}, \tag{3.6}$$

which can be written more compactly as

$$\boldsymbol{w}(\boldsymbol{x}) - \chi(\boldsymbol{x}) \mathcal{G}_{\mathrm{bdy}}\{\boldsymbol{w}\} = \chi(\boldsymbol{x}) \boldsymbol{E}^{\mathrm{bkg}}(\boldsymbol{x}) \quad \text{for } \boldsymbol{x} \in \mathbb{D}, \tag{3.7}$$

where the linear operator $\mathcal{G}_{\mathrm{bdy}}$ is implicitly defined in Equation (3.6).

To summarize, the two fundamental unknowns in CSI-EPT are the contrast function χ and the contrast source $\boldsymbol{w}$ and the basic CSI-EPT equations are the data equation (Equation (3.4)) and the object equation (Equation (3.7)).

Now suppose we have an approximation for the contrast function and contrast source available. We denote these approximants by $\tilde{\chi}$ and $\tilde{\boldsymbol{w}}$, respectively, and in order to measure how well these approximations satisfy the data and object equations, we introduce the data and object residuals as

$$r_{\mathrm{dat}}(\boldsymbol{x}) = B_1^{+;\mathrm{sca}}(\boldsymbol{x}) - \mathcal{G}_{\mathrm{dat}}\{\tilde{\boldsymbol{w}}\}(\boldsymbol{x}) \quad \text{for } \boldsymbol{x} \in \mathbb{D}, \tag{3.8}$$

and

$$\boldsymbol{r}_{\mathrm{obj}}(\boldsymbol{x}) = \tilde{\chi}(\boldsymbol{x}) \boldsymbol{E}^{\mathrm{bkg}}(\boldsymbol{x}) - \tilde{\boldsymbol{w}}(\boldsymbol{x}) + \tilde{\chi}(\boldsymbol{x}) \mathcal{G}_{\mathrm{bdy}}\{\tilde{\boldsymbol{w}}\}(\boldsymbol{x}) \quad \text{for } \boldsymbol{x} \in \mathbb{D}, \tag{3.9}$$

respectively, and measure their magnitudes using the L_2-norms

$$\|r_{\mathrm{dat}}\|_{\mathbb{D}}^2 = \int_{\boldsymbol{x} \in \mathbb{D}} |r_{\mathrm{dat}}(\boldsymbol{x})|^2\, \mathrm{d}V \quad \text{and} \quad \|\boldsymbol{r}_{\mathrm{obj}}\|_{\mathbb{D}}^2 = \int_{\boldsymbol{x} \in \mathbb{D}} |\boldsymbol{r}_{\mathrm{obj}}(\boldsymbol{x})|^2\, \mathrm{d}V. \tag{3.10}$$

In CSI-EPT, these norms are used to define the objective function

Listing 3.1. Contrast Source Inversion - EPT (CSI-EPT)

- Given initial guesses $\tilde{\chi}^{[0]}$ and $\tilde{\boldsymbol{w}}^{[0]}$ for the contrast function and contrast source, respectively
- For $k = 1, 2, \ldots$
  1. Fix the contrast to $\tilde{\chi}^{[k-1]}$ and update the contrast source according to the update formula
  $$\tilde{\boldsymbol{w}}^{[k]} = \tilde{\boldsymbol{w}}^{[k-1]} + \alpha^{[k]} \boldsymbol{v}^{[k]}.$$
  2. Compute the corresponding electric field strength $\boldsymbol{E}^{[k]}$ according to (cf. Equation (3.5))
  $$\tilde{\boldsymbol{E}}^{[k]}(\boldsymbol{x}) = \boldsymbol{E}^{\mathrm{bkg}}(\boldsymbol{x}) + \mathcal{G}_{\mathrm{bdy}}\{\tilde{\boldsymbol{w}}^{[k]}\}(\boldsymbol{x}).$$
  3. Knowing the contrast source $\tilde{\boldsymbol{w}}^{[k]}$ and the corresponding electric field strength $\tilde{\boldsymbol{E}}^{[k]}$, determine the contrast function $\tilde{\chi}^{[k]}$ from the constitutive relation $\tilde{\boldsymbol{w}}^{[k]} = \tilde{\chi}^{[k]} \tilde{\boldsymbol{E}}^{[k]}$ by solving the least-squares problem $\|\tilde{\chi}\tilde{\boldsymbol{E}}^{[k]} - \tilde{\boldsymbol{w}}^{[k]}\|^2_{\mathbb{D}}$ for the minimum norm contrast function $\tilde{\chi}$.
  4. Stop if objective function is smaller than user specified tolerance level, or if maximum number of iterations has been reached.
- End

$$F(\tilde{\chi}, \tilde{\boldsymbol{w}}) = \frac{\|r_{\mathrm{dat}}\|^2_{\mathbb{D}}}{\|B_1^{+;\mathrm{sca}}\|^2_{\mathbb{D}}} + \frac{\|\boldsymbol{r}_{\mathrm{obj}}\|^2_{\mathbb{D}}}{\|\tilde{\chi}\boldsymbol{E}^{\mathrm{bkg}}\|^2_{\mathbb{D}}} \tag{3.11}$$

and the goal is to find a contrast function and contrast source that minimizes this objective function. We note that including the 2-norm of the object residual in the objective function (second term on the right-hand side of Equation (3.11)) is crucial to the success of CSI, since it has been shown that a contrast source inversion approach without this term produces unsatisfactory results in general [24].

In CSI-EPT, finding the desired contrast function is now realized by minimizing the objective function in a "fix-one-minimize-for-the-other" approach. The iterative process is continued until a predefined maximum number of iterations or specified tolerance level of the objective function has been reached. Specifically, the basic CSI-EPT algorithm is as shown in Listing 3.1.

Polak-Ribière update directions are usually taken for the update direction $\boldsymbol{v}^{[k]}$ in Step 1 of the algorithm, but Fletcher-Reeves or Hesteness-Stiefel update directions may be used as well. To determine these update directions, the gradient of $F(\tilde{\chi}^{[k-1]}, \tilde{\boldsymbol{w}})$ with respect to $\tilde{\boldsymbol{w}}$ at $\tilde{\boldsymbol{w}} = \tilde{\boldsymbol{w}}^{[k-1]}$ is required. Explicit expressions for this gradient and the

corresponding step length $\alpha^{[k]}$ can be found in [23], for example.

Also note that with Equation (3.5), the object residual can be written as $\boldsymbol{r}_{\text{obj}} = \tilde{\chi}\tilde{\boldsymbol{E}} - \tilde{\boldsymbol{w}}$ and in Steps 2 and 3 we find the minimum-norm contrast function $\tilde{\chi}$ for which $\|\boldsymbol{r}_{\text{obj}}\|^2_{\mathbb{D}}$ is minimized. This contrast function is generally sensitive to small perturbations in $\tilde{\boldsymbol{w}}$ at locations where the magnitude of the electric field strength is "small." To suppress this effect, we can alternatively update the contrast function at every iteration according to the update formula

$$\tilde{\chi}^{[k]} = \tilde{\chi}^{[k-1]} + \beta^{[k]} d^{[k]}, \tag{3.12}$$

with $d^{[k]}$ the Polak-Ribière update direction for the contrast function and $\beta^{[k]}$ its corresponding update coefficient. Such an approach usually has a regularizing effect and typically leads to smoother reconstructions.

3.2.1. THE OBJECT AND DATA OPERATORS IN THREE-DIMENSIONAL CSI-EPT

In three dimensions and with air as a background medium, the integral representations for the scattered fields as given by Equation (3.2) take on the form

$$\boldsymbol{B}^{\text{sca}}(\boldsymbol{x}) = \mathrm{j}\frac{\omega}{c_0^2}\boldsymbol{\nabla}\times\boldsymbol{A}^{\text{sca}}(\boldsymbol{x}) \quad \text{and} \quad \boldsymbol{E}^{\text{sca}}(\boldsymbol{x}) = (k_0^2 + \boldsymbol{\nabla}\boldsymbol{\nabla}\cdot)\boldsymbol{A}^{\text{sca}}(\boldsymbol{x}), \tag{3.13}$$

where c_0 is the electromagnetic wave speed in vacuum, $k_0 = \omega/c_0$ the wave number in vacuum, and $\boldsymbol{A}^{\text{sca}}$ is the vector potential given by

$$\boldsymbol{A}^{\text{sca}}(\boldsymbol{x}) = \int_{\boldsymbol{x}'\in\mathbb{D}} G(\boldsymbol{x}-\boldsymbol{x}')\,\boldsymbol{w}(\boldsymbol{x}')\,\mathrm{d}V, \tag{3.14}$$

with G the three-dimensional Green's function of the vacuum background domain given by

$$G(\boldsymbol{x}) = \frac{\exp(-\mathrm{j}k_0|\boldsymbol{x}|)}{4\pi|\boldsymbol{x}|}. \tag{3.15}$$

Note that the nabla-operators act on the position vector $\boldsymbol{x}$ and not on the integration variable $\boldsymbol{x}'$. The 3D object operator $\mathcal{G}_{\text{bdy}}$ can be easily identified from the second equation in Equation (3.13). For the data operator $\mathcal{G}_{\text{dat}}$, however, we have to substitute the x- and y-components of the scattered magnetic flux density in Equation (3.3) to obtain

$$B_1^{+;\text{sca}} = \frac{\omega}{c_0^2}\left(\partial^+ A_z^{\text{sca}} - \partial_z A^{+;\text{sca}}\right), \tag{3.16}$$

where $\partial^+ = \frac{1}{2}(\partial_x + \mathrm{j}\partial_y)$ and $A^{+;\text{sca}} = \frac{1}{2}(A_x^{\text{sca}} + \mathrm{j}A_y^{+;\text{sca}})$. From the above expression for the scattered B_1^+-field, the 3D data operator $\mathcal{G}_{\text{dat}}$ can be identified. Note the particular structure of this operator: the scattered B_1^+-field originates from a difference between the transverse variations of the longitudinal vector potential ($\partial^+ A_z^{\text{sca}}$) and the longitudinal variations of the transverse vector potential ($\partial_z A^{+;\text{sca}}$).

3.2.2. THE OBJECT AND DATA OPERATORS IN TWO-DIMENSIONAL CSI-EPT

In various papers (see [25], for example) it has been reported that the radiofrequency (RF) field in the midplane of a birdcage coil is essentially E-polarized, meaning that the electric field strength has a longitudinal component only ($\boldsymbol{E} = E_z \mathbf{i}_z$), while the magnetic flux density has only x- and y-components ($\boldsymbol{B} = B_x \mathbf{i}_x + B_y \mathbf{i}_y$). Additionally, in a two-dimensional configuration that is invariant in the z-direction, external electric current densities with longitudinal components only generate E-polarized fields. Identifying the currents in the rungs of the birdcage coil with these z-directed external current sources and denoting the slice through the object that coincides with the midplane of the birdcage coil by $\mathbb{A}$, it makes sense to assume that within this midplane the RF field is essentially two-dimensional and E-polarized with integral representations for the scattered fields given by

$$\boldsymbol{B}^{\text{sca}}(\boldsymbol{\rho}) = \mathrm{j}\frac{\omega}{c_0^2}\boldsymbol{\nabla}_{\text{T}} \times \boldsymbol{A}^{\text{sca}}(\boldsymbol{\rho}), \quad \text{and} \quad \boldsymbol{E}^{\text{sca}}(\boldsymbol{\rho}) = k_0^2 \boldsymbol{A}^{\text{sca}}(\boldsymbol{\rho}), \tag{3.17}$$

where $\boldsymbol{\rho}$ is the position vector in the midplane of the birdcage coil, $\boldsymbol{\nabla}_{\text{T}} = \mathbf{i}_x \partial_x + \mathbf{i}_y \partial_y$ is the transverse nabla-operator, and

$$\boldsymbol{A}^{\text{sca}}(\boldsymbol{\rho}) = \int_{\boldsymbol{\rho}' \in \mathbb{A}} G(\boldsymbol{\rho} - \boldsymbol{\rho}')\, \boldsymbol{w}(\boldsymbol{\rho}')\, \mathrm{d}S \tag{3.18}$$

is the vector potential in two dimensions (and is thus expressed as a two-dimensional integral as opposed to the three-dimensional integral in the 3D case) with

$$G(\boldsymbol{\rho}) = -\frac{\mathrm{j}}{4} H_0^{(2)}(k_0 |\boldsymbol{\rho}|) \tag{3.19}$$

the Green's function of the two-dimensional homogeneous background medium (air) and $H_0^{(2)}$ is the Hankel function of the second kind and order zero. In this two-dimensional case, the object operator $\mathcal{G}_{\text{bdy}}$ can be easily identified from the second equation of Equation (3.17) and does not contain a gradient-divergence operator as in the three-dimensional case. For the 2D data operator $\mathcal{G}_{\text{dat}}$, we have to substitute the x- and y-components of the magnetic flux density as given by the first equation of Equation (3.17) in the definition of the B_1^+-field to obtain

$$B_1^{+;\text{sca}} = \frac{\omega}{c_0^2} \partial^+ A_z^{\text{sca}}. \tag{3.20}$$

From this expression, the 2D data operator $\mathcal{G}_{\text{dat}}$ can now easily be identified. Comparing the two-dimensional field representation of Equation (3.20) with its three-dimensional counterpart of Equation (3.16), we observe that longitudinal spatial variations are absent in the two-dimensional case. Moreover, the vector potentials in both expressions are different as well, since this quantity is computed using Equation (3.18) in the two-dimensional case, while the three-dimensional vector potential is given by Equation (3.14). The differences between two- and three-dimensional CSI-EPT reconstructions will be discussed further in Section 3.3.

3.2.3. TWO-DIMENSIONAL CSI-EPT SIMPLIFIED – FIRST-ORDER INDUCED CURRENT EPT (FOIC-EPT)

In two dimensions, the CSI-EPT algorithm can be simplified by exploiting the particular structure of E-polarized RF fields. To make this simplification explicit, we first introduce the differentiation operator $\partial^- = \frac{1}{2}(\partial_x - \mathrm{j}\partial_y)$ and note that the operators ∂^- and ∂^+ essentially factor the two-dimensional Laplacian $\Delta = \partial_x^2 + \partial_y^2$ as

$$\Delta = 4\partial^-\partial^+ = 4\partial^+\partial^-. \tag{3.21}$$

Now as a first step, we substitute the second equation of Equation (3.17) in Equation (3.20) to obtain

$$B_1^{+;\mathrm{sca}}(\boldsymbol{\rho}) = \frac{1}{\omega}\partial^+ E_z^{\mathrm{sca}}(\boldsymbol{\rho}). \tag{3.22}$$

Subsequently, we use the definition of the scattered fields to write the above expression as

$$B_1^{+}(\boldsymbol{\rho}) = B_1^{+;\mathrm{bkg}}(\boldsymbol{\rho}) + \frac{1}{\omega}\partial^+ E_z(\boldsymbol{\rho}) - \frac{1}{\omega}\partial^+ E_z^{\mathrm{bkg}}(\boldsymbol{\rho}) \tag{3.23}$$

and since $B_1^{+;\mathrm{bkg}}(\boldsymbol{\rho}) = \frac{1}{\omega}\partial^+ E_z^{\mathrm{bkg}}(\boldsymbol{\rho})$, this simplifies to

$$B_1^{+}(\boldsymbol{\rho}) = \frac{1}{\omega}\partial^+ E_z(\boldsymbol{\rho}). \tag{3.24}$$

If we now act with the ∂^- operator on this equation, we obtain

$$\partial^- B_1^{+} = \frac{1}{4\omega}\Delta E_z \tag{3.25}$$

and since E_z satisfies $\Delta E_z - \mathrm{j}\omega\mu_0 J_z^{\mathrm{ind}} = 0$ with

$$J_z^{\mathrm{ind}} = (\sigma + \mathrm{j}\omega\varepsilon)E_z, \tag{3.26}$$

we arrive at

$$J_z^{\mathrm{ind}} = \frac{4}{\mathrm{j}\mu_0}\partial^- B_1^{+}. \tag{3.27}$$

This last equation shows that in two dimensions, the induced current density is obtained (accounting for multiplication by $4/\mathrm{j}\mu_0$) by acting with the ∂^- operator on the total B_1^+-field. The simplified CSI-EPT method is therefore called a first-order induced current EPT method, since a first-order differentiation of the B_1^+-field essentially immediately results in an image of the induced current density.

As shown in [20], after the induced current density has been obtained, the corresponding electric field strength can be computed by solving a specific integral equation defined on $\mathbb{A}$. With the electric field strength now known, the conductivity and permittivity profiles within the slice can be obtained from Equation (3.26). The overall first-order induced current density EPT algorithm can be summarized as presented in Listing 3.2.

Listing 3.2. First-Order Induced Current EPT Algorithm (foIC-EPT)

- Given the measured B_1^+-field in the midplane of the birdcage coil:
  1. Determine the induced current density using Equation (3.27).
  2. Determine the corresponding electric field strength by solving a specific integral equation (Equation (12) in [20]).
  3. Knowing the induced current density and the electric field strength, determine the conductivity and permittivity profiles using Equation (3.26).

Further details about this algorithm can be found in [20]. Finally, we note that the above algorithm is a direct non-iterative EPT method and, as opposed to CSI-EPT, requires the solution of a system of equations (Step 2) to arrive at the reconstructed conductivity and permittivity profiles. Fortunately, as demonstrated in [20], this system of equations can be solved efficiently using iterative solvers such as the generalized minimal residual method (GMRES) [29] and typically only a small number of iterations is required to reach a prescribed error.

3.3. METHODS AND RESULTS

To illustrate the performance of foIC-EPT and two- and three-dimensional CSI-EPT, we reconstruct the conductivity and permittivity profiles of the head of the anatomical human body model Duke from the Virtual Family [27] (see Figures 3.1a and 3.1b), from noise-free B_1^+-data. The head model consists of $124 \times 100 \times 109$ isotropic voxels with side lengths of 2 mm. The model is placed inside an ideal high-pass birdcage coil (see Figure 3.1a) consisting of 16 rungs each having a width of 25 mm. The coil has a radius of 150 mm, is 195 mm long, and is driven in quadrature at 128 MHz, which corresponds to the operating frequency of a 3 T MRI system. The shield surrounding the coil has a radius of 180 mm and a length of 200 mm. Commercial EM simulation software (XFdtd, v.7.5, Remcom State College, PA, USA) is used to obtain the background field $\{\boldsymbol{E}^{\text{bkg}}, \boldsymbol{B}^{\text{bkg}}\}$ as generated by the high-pass birdcage coil. Finally, to investigate the difference between two- and three-dimensional conductivity and permittivity reconstructions, we also consider a longitudinally uniform "head model" in which the center slice is simply repeated in the longitudinal direction thereby creating a model with no variations in the longitudinal z-direction within the head (see Figure 3.1c).

3.3.1. TWO-DIMENSIONAL CSI-EPT AND FOIC-EPT

The CSI-EPT method was originally implemented for two-dimensional configurations in [14] to study its potential as an EPT reconstruction method and to test if the method can handle strongly inhomogeneous tissue profiles. Let us therefore start with a purely two-dimensional reconstruction problem in which we attempt to reconstruct the conductivity and permittivity profiles within the center slice of the head model shown in

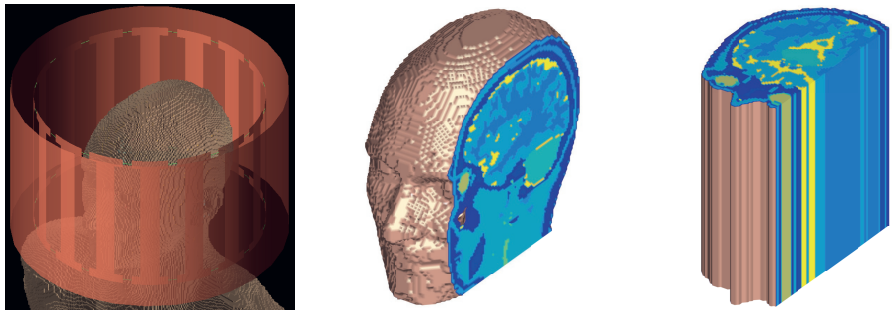

(a) (b) (c)

Figure 3.1: Birdcage coil and head models. The high-pass birdcage coil with the head model placed inside (a), the Duke head model from the Virtual Family [27] (b), and a longitudinally uniform head model obtained by repeating the center slice in the longitudinal direction (c).

Figure 3.2a. In this two-dimensional setting, we take the background field in the mid-plane of the realistic birdcage coil shown in Figure 3.1a as the 2D background field. The reconstructed conductivity and permittivity profiles obtained after 5000 iterations of the two-dimensional CSI-EPT method are shown in Figure 3.2b. It takes the algorithm approximately 86 seconds on an Intel i7-6700 CPU operating on Windows 7 with Matlab 2016a to arrive at these reconstructions and we terminate the algorithm after 5000 iterations, since the objective function has already dropped below a 1.53×10^{-5} tolerance level at this point and essentially no significant improvements are obtained. In addition, the foIC-EPT reconstruction profiles of the conductivity and permittivity are shown in Figure 3.2c and the errors of CSI-EPT and foIC-EPT conductivity and permittivity reconstructions are shown in Figure 3.2d and Figure 3.2e, respectively. We observe that the quality of the foIC-EPT reconstructions is similar to CSI-EPT even though it takes foIC-EPT only a fraction of a second to produce these reconstructions (see Table 3.1 for details).

3.3.2. THREE-DIMENSIONAL CSI-EPT

In a two-dimensional approach, the RF field is E-polarized with an electric field strength that is longitudinal ($\boldsymbol{E} = E_z \mathbf{i}_z$) and a magnetic flux density that is transverse ($\boldsymbol{B} = B_x \mathbf{i}_x + B_y \mathbf{i}_y$). Such an approach has been shown to be reasonable for a homogeneous cylindrical phantom in a central region of a body coil consisting of elementary center-fed dipole antennas in [25], and indeed, when the longitudinally uniform head model of Figure 3.1c is placed within our birdcage coil we also observe that the x- and y- components of the electric field strength in the central transverse slice are small compared to its z-component as illustrated in the top rows of Figures 3.3a–c and Figures 3.4a–b.

However, as we move away from the center slice in the longitudinally uniform head model of Figure 3.1c, the magnitude of the x- and y-components of the electric field strength starts to increase as illustrated in the top rows of Figures 3.3d–f and Figures 3.4c–d, where the magnitude of the electric field strength components is shown in a slice located 5 cm above the central slice. We observe that even though the trans-

Table 3.1: The mean and standard deviation of the reconstructed electrical properties in the different tissues that are apparent in the center slice of the head models using 2D CSI-EPT and foIC-EPT in a two-dimensional setting. Units of σ and ε_r are in siemens per meter and permittivity of free space, respectively.

	Conductivity (σ)			Relative permittivity (ε_r)		
	True	2D CSI-EPT	foIC-EPT	True	2D CSI-EPT	foIC-EPT
Fat	0.07	0.13±0.10	0.18±0.10	12.37	17.23±7.89	19.27±7.15
Red marrow	0.16	0.11±0.06	0.15±0.03	13.54	11.08±2.52	13.68±1.47
Bone	0.07	0.14±0.15	0.21±0.14	14.72	19.09±8.05	21.73±6.90
Eye lens	0.31	0.54±0.11	0.78±0.09	42.79	48.86±5.26	51.52±1.44
Nerve	0.35	0.74±0.30	0.77±0.26	44.07	51.49±8.74	47.33±7.42
Connective tissue	0.50	0.47±0.12	0.44±0.13	51.86	46.48±7.56	40.54±7.06
White matter	0.34	0.36±0.04	0.38±0.04	52.53	54.33±3.12	55.37±3.54
Muscle	0.72	0.63±0.11	0.55±0.13	63.49	56.76±7.28	48.30±8.72
Eye sclera	0.92	0.89±0.15	0.87±0.13	65.00	56.78±6.67	50.26±5.95
Skin	0.52	0.48±0.08	0.36±0.09	65.44	59.00±8.95	42.29±8.55
Hypothalamus	0.80	0.88±0.11	0.91±0.11	66.78	59.48±4.91	54.12±4.20
Eye vitreous humor	1.51	1.46±0.13	1.40±0.15	69.06	66.19±4.86	61.03±4.95
Cornea	1.06	0.92±0.13	0.83±0.11	71.46	61.52±9.32	52.81±5.84
Gray matter	0.59	0.61±0.15	0.63±0.15	73.52	72.68±4.18	70.54±4.92
Midbrain	0.83	0.84±0.17	0.88±0.18	79.74	78.58±10.24	81.93±12.33
Cerebrospinal fluid	2.14	1.90±0.29	1.75±0.29	84.04	80.66±8.57	76.46±11.31
Mucosa	2.28	1.50±0.03	1.01±0.02	116.00	78.07±5.17	53.83±2.77

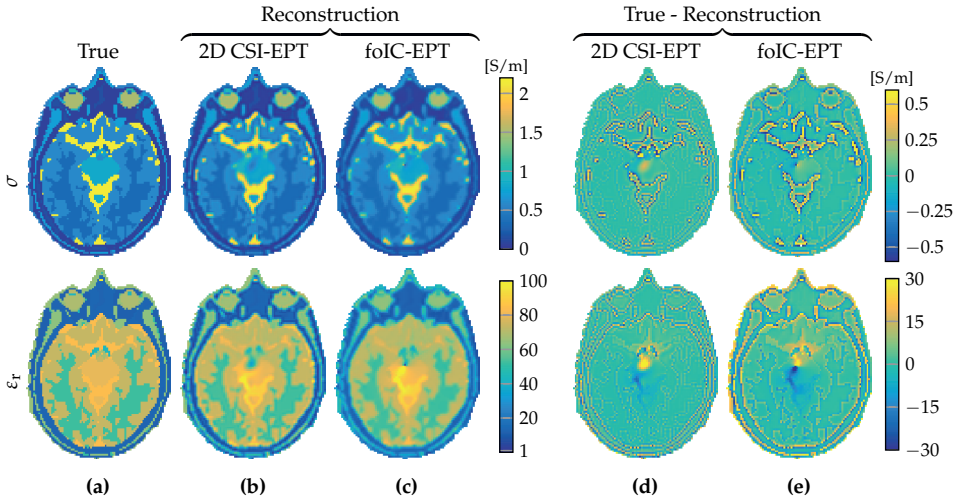

Figure 3.2: Reconstruction results from 2D reconstruction methods. The true model (a), the reconstruction obtained after 5000 iterations of 2D CSI-EPT (b) and the reconstruction from foIC-EPT (c). The respective errors are shown in (d, e). Top row shows the conductivity and the bottom row the relative permittivity.

verse components of the electric field strength are negligible within the center slice, they can no longer be neglected 5 cm away from it.

Furthermore, for the realistic heterogeneous head model of Figure 3.1b a two-dimensional E-polarized field assumption completely fails as shown in the bottom rows of Figures 3.3a–f and 3.4a–d. In the slice 5 cm above the central slice and even within the central slice itself the x- and y-components of the electric field strength can no longer be neglected and have to be taken into account in the full Maxwell equations to properly describe RF field behavior within the head model.

To study the effects of longitudinal spatial variations of the tissue parameters on the B_1^+-field, we consider Equation (3.16) again and write it in the form

$$B_1^{+;\mathrm{sca}} = \mathcal{B}^{\mathrm{tra}} + \mathcal{B}^{\mathrm{lon}}, \tag{3.28}$$

where $\mathcal{B}^{\mathrm{tra}} = \frac{\omega}{c_0^2}\partial^+ A_z^{\mathrm{sca}}$ and $\mathcal{B}^{\mathrm{lon}} = -\frac{\omega}{c_0^2}\partial_z A^{+;\mathrm{sca}}$. The longitudinal variation term $\mathcal{B}^{\mathrm{lon}}$ is absent in a 2D approach (see Equation (3.20)), since in a 2D setting the configuration is assumed to be invariant in the longitudinal z-direction ($\partial_z = 0$). Figure 3.5, however, shows that for both the longitudinally homogeneous and realistic heterogeneous head model the longitudinal variation term is significant and cannot be ignored. Especially near the periphery of both head models, $\mathcal{B}^{\mathrm{lon}}$ contributes to the scattered B_1^+-field. More specifically, within a 1 cm outer boundary layer located in the center slice, the mean of the fraction $|\mathcal{B}^{\mathrm{lon}}/B_1^{+;\mathrm{sca}}|$ is 1.18 and 1.25 for the homogeneous and inhomogeneous head model, respectively, while in the inner region these means are 0.51 and 0.60 and similar averages are obtained for the slice located 5 cm above the center slice. From these observations, it is clear that longitudinal variations of the transverse vector potential $A^{+;\mathrm{sca}}$ contribute to the scattered B_1^+-field and cannot be ignored.

Up to this point, we have compared 3D RF field structures with their 2D coun-

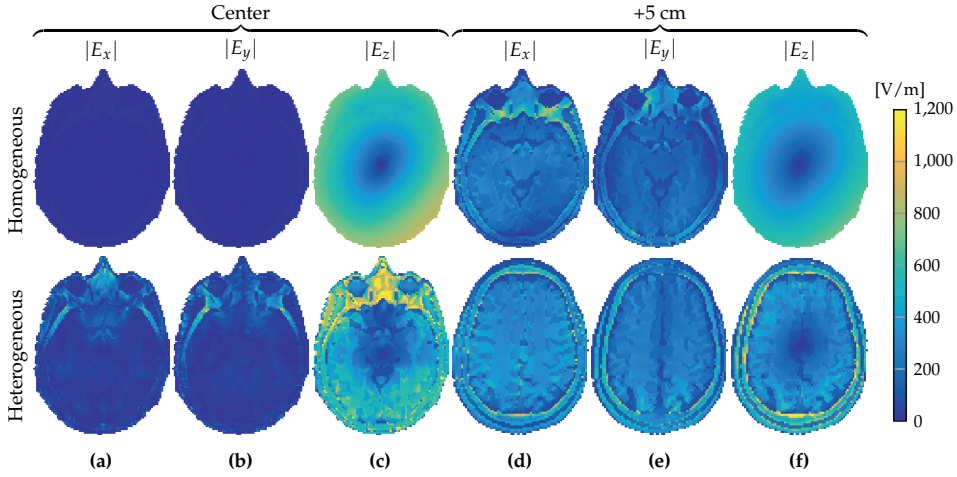

Figure 3.3: The magnitude of the electric field strength components. The x-, y- and z-component at the transversal midplane (a-c) and at the slice 5 cm higher (d-f), respectively. The top and bottom row show the fields in the case of a longitudinal homogeneous and heterogeneous object, respectively.

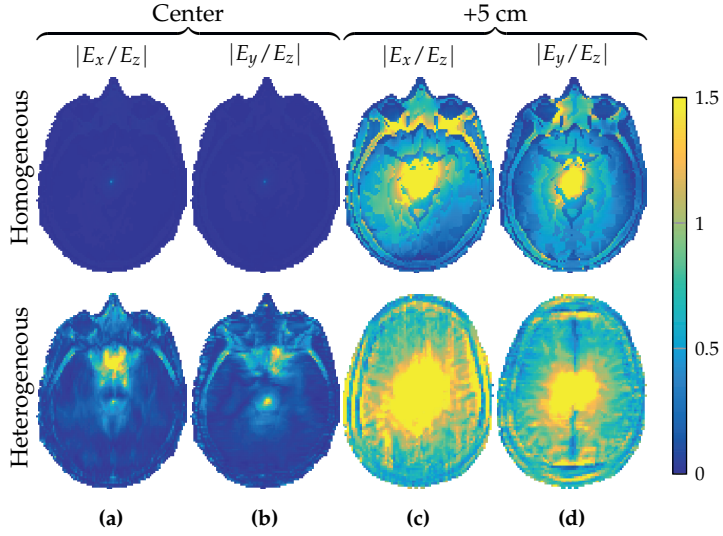

Figure 3.4: Ratios of the x- and y-components of the electric field strength relative to its z-component. The relative field components at the center slice (a,b) and at the slice 5 cm higher (c,d). The top row is for the longitudinally uniform object, the bottom row for the object with longitudinal variations.

terparts for a longitudinally uniform and a realistic heterogeneous head model. In a two-dimensional configuration, however, the sources are invariant in the longitudinal direction as well and we expect that due to the finite extent of the birdcage coil additional deviations in the B_1^+ fields will be observed.

To investigate this issue further, we first determine the two-dimensional B_1^+-field in the central slice as described in Section 3.3.1. The magnitude and phase of this field

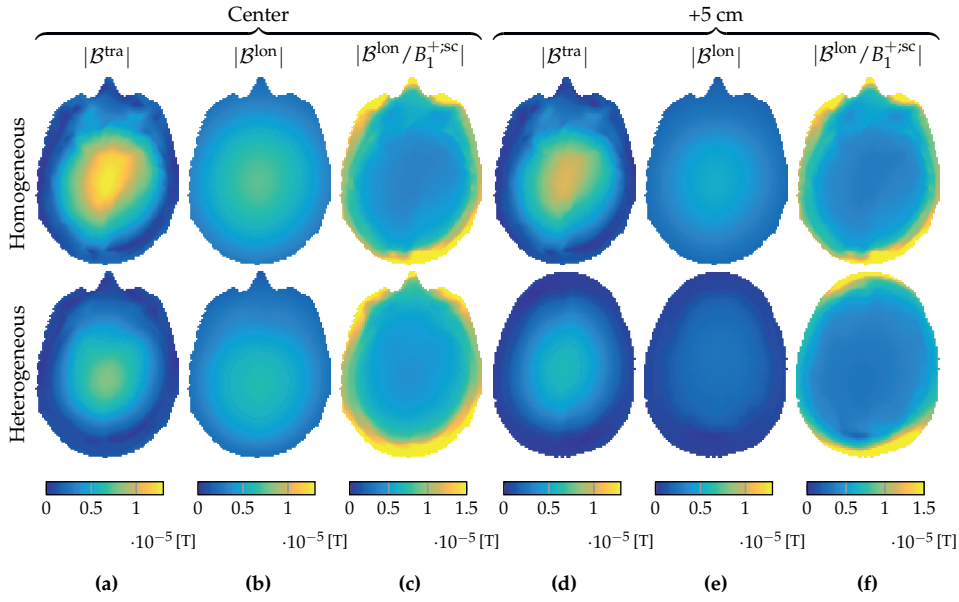

Figure 3.5: Magnitude of the scattered B_1^+ terms. The transverse variation (a) and longitudinal variation term of the scattered B_1^+ (b) and the contributions of $\mathcal{B}^{\mathrm{lon}}$ w.r.t. $B_1^{+;\mathrm{sca}}$ (c) at the center slice. (d-f) show respectively the same at a slice 5 cm higher in the head domain. Top row shows in the case of a longitudinally uniform object, the bottom row for the head model with longitudinal variations. (b) and (e) are neglected in the 2D approach.

are shown in the top and bottom row of Figure 3.6a, respectively. Subsequently, we consider RF excitation by the 3D birdcage coil, but assume that the birdcage coil, including its currents, does not vary in the longitudinal direction. For the longitudinally uniform head model, a B_1^+-field as shown in Figure 3.6b is then obtained and we observe that this field strongly resembles the 2D B_1^+-field pattern of Figure 3.6a. Replacing the longitudinal invariant currents in the rungs by the exact current, but keeping the homogeneous head model, we obtain the B_1^+-field pattern shown in Figure 3.6c. The agreement with the 2D field B_1^+-field pattern clearly deteriorates and this correspondence becomes even worse for the realistic longitudinal heterogeneous head model as shown in Figure 3.6d. Since the B_1^+-field is used as an input for the CSI-EPT method, an accurate correspondence is obviously necessary for a proper reconstruction. The 2D CSI-EPT algorithm expects a 2D B_1^+-field as shown in Figure 3.6a for the center head slice, but in 3D the B_1^+-field from Figure 3.6d is present and providing this 3D field as an input to a 2D CSI-EPT algorithm will lead to inaccurate reconstructions in general.

To illustrate how these differences in actual fields (3D) and expected fields (2D) translate to reconstruction errors, both two-dimensional algorithms have been applied to quasi three-dimensional data using either 3D amplitudes or phases. Note that, in order to match 2D and 3D data, the maximum absolute value of the B_1^+-field of both datasets is taken to be equal. The results are depicted in Figure 3.7b–e from which it can be observed that particularly the permittivity is sensitive to 2D violations. This reconstruction difference between conductivity and permittivity is due to the fact that

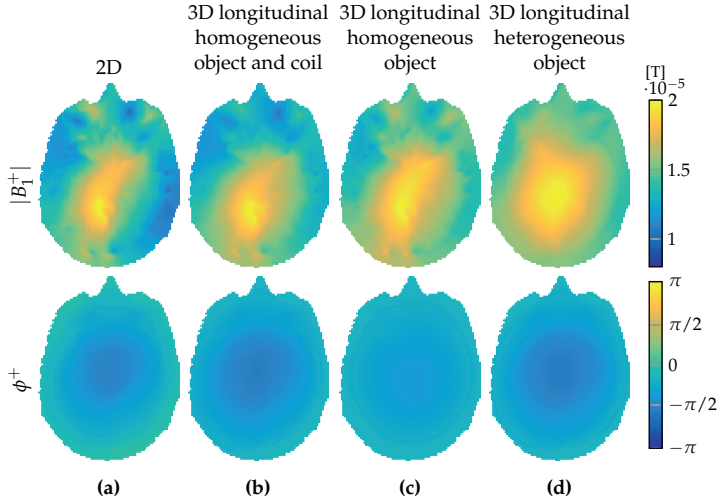

Figure 3.6: B_1^+ field comparison. The total B_1^+ field assumed in the 2D setting (a), the total B_1^+ field obtained in a 3D setting with longitudinal homogeneity of the object and coil (b), of longitudinal homogeneity of only the object (c) and with longitudinal variations of also the object (d). Top row shows the B_1^+ magnitude, the bottom row the B_1^+ phase.

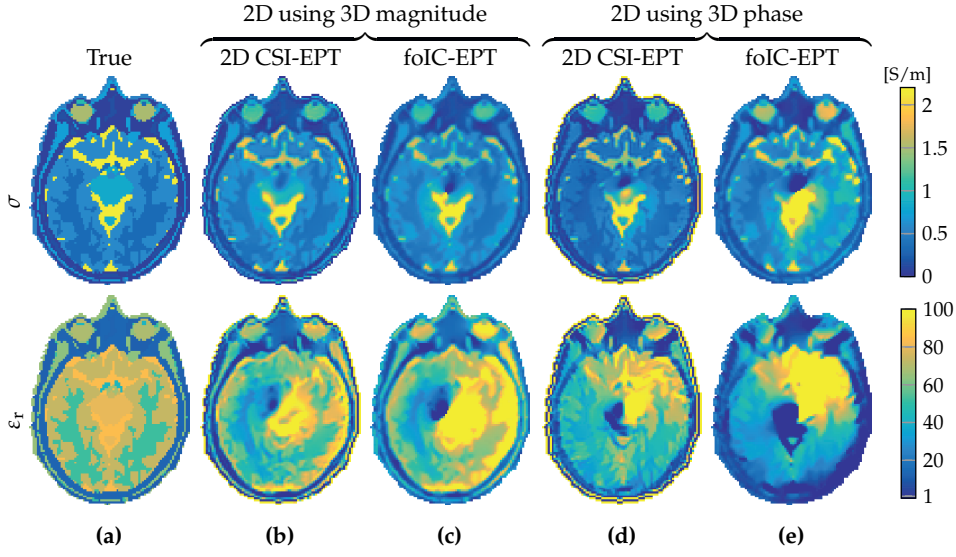

Figure 3.7: Reconstruction results from 2D reconstruction methods using parts of 3D B_1^+ data. True model (a), reconstruction results assuming 2D phase with 3D magnitude (b,c), and reconstruction results assuming 2D magnitude with 3D phase (d,e) of the B_1^+-field in the central transverse slice from simulations with the longitudinal invariant head model. Top row shows the conductivity and the bottom row the relative permittivity.

conduction currents ($\sigma \boldsymbol{E}$) influence the B_1^+-field to a much larger extent than the displacement currents ($j\omega\varepsilon\boldsymbol{E}$) at 3 T.

The reconstructions of the conductivity and relative permittivity profiles for the full 3D case without any further assumptions, using 3D magnitude as well 3D phase B_1^+ data are shown for the longitudinally uniform model in Figures 3.8a–f and for the realistic heterogeneous head model in Figures 3.8g–l. Reconstructions are shown for the central slice profiles as well as for the profiles located within the slice positioned 5 cm above the central slice. For comparison, 2D CSI-EPT reconstructions based on 3D B_1^+ data are also presented. The relative residual error (norm of the difference between the exact and reconstructed profile normalized by the norm of the exact profile, where the norm is taken over the center slice) of Figure 3.8h is 0.7339 and 0.8263 for the conductivity and permittivity, respectively, while the relative residual error of the conductivity and permittivity of Figure 3.8i is 0.3358 and 0.1587, respectively. Clearly, 2D CSI-EPT is unable to accurately reconstruct the conductivity and permittivity profiles. The 2D and 3D permittivity reconstructions are also less accurate than the conductivity reconstructions, indicating that B_1^+-field data acquired at 3 T is less sensitive to permittivity variations.

Finally, to emphasize that 3D CSI-EPT is a fully three-dimensional volumetric reconstruction method, we present a full 3D CSI-EPT reconstruction of the realistic head model obtained after 50000 iterations based on 3D B_1^+ data, in Figure 3.9. This number of iterations was chosen due to time constraints, since it takes approximately 110 hours on an Intel i7-6700 CPU operating on Windows 7 with Matlab 2016a.

3.4. DISCUSSION

We have investigated the performance of two- and three-dimensional CSI-EPT in reconstructing dielectric tissue profiles based on B_1^+ data collected inside the reconstruction slice or domain of interest. Since this data has its support inside the reconstruction domain, EPT belongs to the class of so-called hybrid inverse problems [8]. In CSI-EPT, reconstructing the tissue parameters is posed as an optimization problem in which an internal objective function, that is an objective function that measures both field and model discrepancies within the domain of interest, is minimized in an iterative manner. Field discrepancies are measured by considering the L_2-norm of the difference between modeled and measured data, while model discrepancies are measured by an L_2-norm that tells us how well a conductivity and permittivity tissue profile and corresponding contrast source satisfy Maxwell's equations. Including model discrepancies in the objective function is crucial to the performance of CSI-EPT, since it has been shown that without this term unsatisfactory reconstruction results may be obtained [24]. In addition to the tissue profiles, CSI-EPT reconstructs the electric field strength as well, and may therefore also be used to predict the SAR that is induced inside the body or a body part of interest [30], which is important for MR safety and hyperthermia treatment planning, for example. Finally, we have also shown that in two dimensions an alternative non-iterative and integral-based reconstruction algorithm called foIC-EPT may be employed. This method is significantly faster than 2D and 3D CSI-EPT and reconstructs the tissue profiles and the corresponding electric field strength essentially in real-time on a present day standard laptop or PC (Intel i5-i7 or similar). However, foIC-EPT is restricted to two-dimensional configurations, since it exploits two-dimensional E-polarized field structures. CSI-EPT, on the other

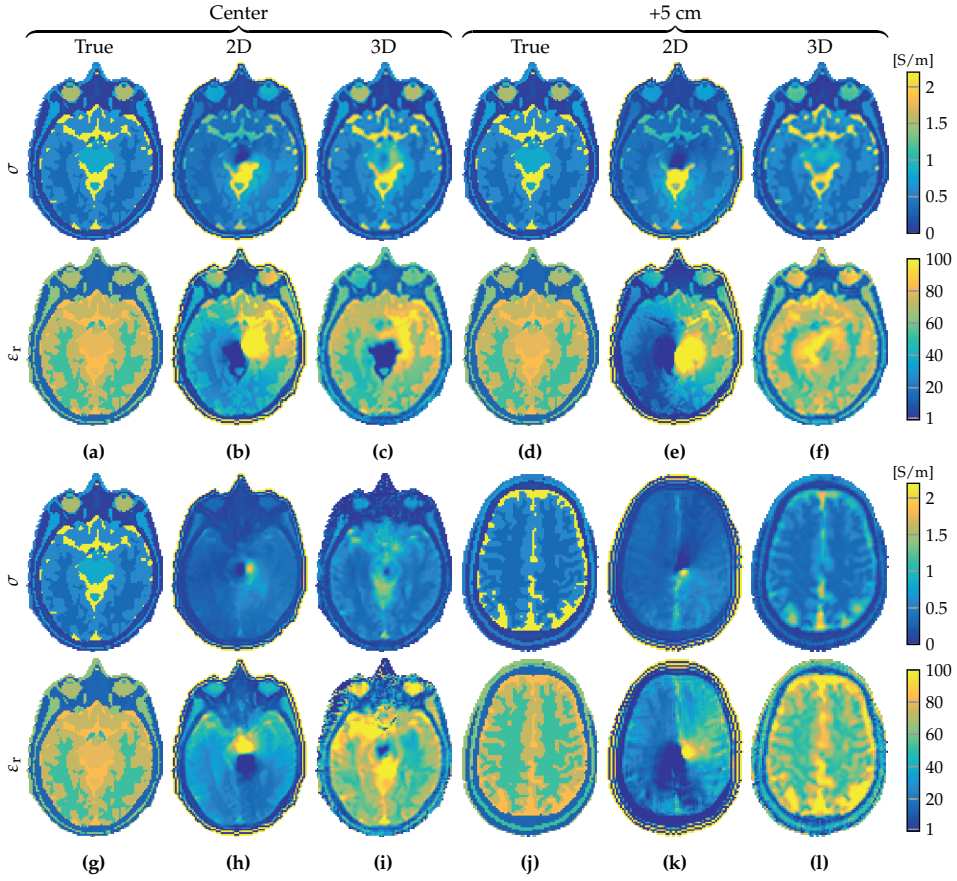

Figure 3.8: Reconstruction comparison of 2D and 3D CSI-EPT on 3D B_1^+ fields after 5000 and 50000 iterations, respectively. (a-c) show the true object, the reconstruction with 2D CSI-EPT and the reconstruction with 3D CSI-EPT for a homogeneous object and for the center slice. (d-f) show respectively the same, but for a slice five centimeter higher. (g-l) show respectively the same as (a-f), but in the case of a longitudinal inhomogeneous object. The top row depicts the conductivity, the bottom row the permittivity.

hand, does not exploit any particular field structure and can be extended to the vectorial three-dimensional case turning CSI-EPT into a volumetric EPT reconstruction method.

We have carried out several comparisons between reconstructions obtained with 2D CSI-EPT, foIC-EPT, and 3D CSI-EPT. Our simulations show that care needs to be exercised when a 2D reconstruction approach is followed, otherwise reconstruction artifacts are obtained in the reconstructed dielectric tissue profiles. Specifically, we have shown that using 2D methods erroneous reconstructions may be obtained, since the longitudinal variations of the transverse vector potential are completely ignored in the data model for the B_1^+ field. Moreover, the vector potential itself is computed differently in 2D and 3D, since longitudinal invariance is assumed in the 2D case. In fact, the transverse electric field and the longitudinal magnetic field vanish in 2D as

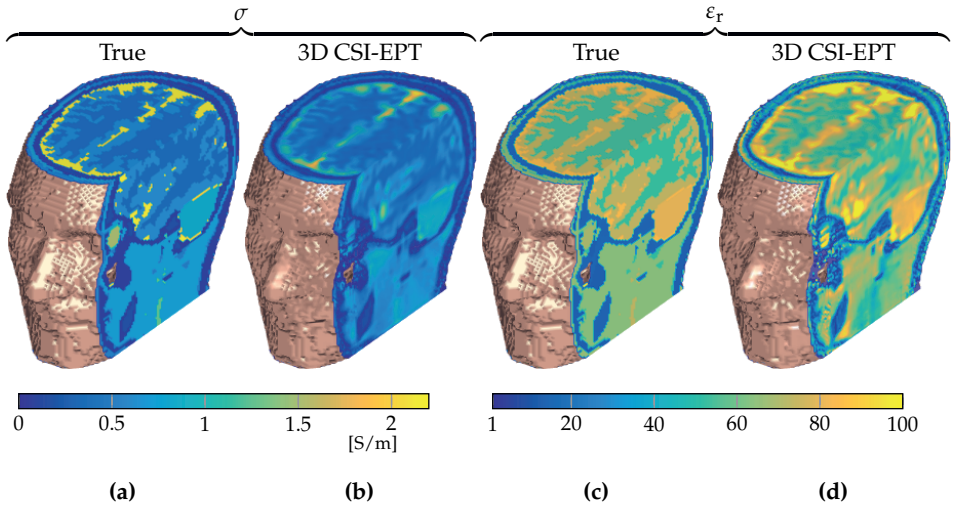

Figure 3.9: Three-dimensional visualization of a section of the 3D CSI-EPT reconstruction of the heterogeneous Duke head model (Figure 3.1b) after 50000 iterations. The true and reconstructed conductivity (a,b) and the true and reconstructed relative permittivity (c,d). The top slice that is visible is the slice 5 cm above the transverse midplane.

a consequence of the (assumed) invariance of the object and external sources along the longitudinal direction. In 3D, however, all components of the electromagnetic field are present and their contributions to the measured data and object equations have to be taken into account. Of course, in some situations an E-polarized field structure may be present in the midplane of a birdcage coil, but the scattered B_1^+-field is also influenced by longitudinal variations of the transverse vector potential ($\partial_z A_z$). These equations can only be simplified to 2D if we can guarantee that longitudinal invariance or smoothness of certain field components can be imposed before any reconstruction algorithm is applied to the measured data. Therefore cylindrical body parts such as the legs or arms might be reliably reconstructed via 2D CSI-EPT, but this at least requires further validation through simulations and measurements using cylindrical phantom models with known dielectric characteristics.

No assumptions on the fields are imposed in 3D CSI-EPT and reconstruction errors due to such assumptions are therefore avoided. Moreover, 3D CSI-EPT is a volumetric reconstruction method and is not restricted to a specific plane within the configuration. Reliable reconstructions can be obtained within any desired domain of interest provided that B_1^+ data is available within this domain. Unfortunately, computation times significantly increase when applying 3D CSI-EPT. Depending on the number of unknowns in the EPT reconstruction problem, 3D CSI-EPT may take many iterations to converge to the desired error tolerance, with total computation times of hours or days even on dedicated computers or servers. In future research, we focus on accelerating the convergence rate of 3D CSI-EPT by including preconditioning techniques in CSI-EPT (as described in [23], for example) that exploit all *a priori* knowledge we have about the object or body part that needs to be reconstructed. This knowledge can also be used to construct an accurate initial guess thereby possibly further accelerating

CSI-EPT.

In our experiments, we have used simulated B_1^+-field data to test the performance of 2D and 3D CSI-EPT on strongly inhomogeneous structures and to study the differences between two- and three-dimensional CSI-EPT approaches. In real-world measurements, the data obviously differs from simulated data and CSI-EPT should be adapted so that it can handle measured B_1^+ data. In this respect, we have identified three practical issues that need to be addressed, which are part of our current CSI-EPT research.

First, in practice the B_1^+-field is obtained in polar form through separate amplitude and phase measurements. In both cases, the collected data is contaminated with noise and therefore filtering or regularization techniques that suppress the effects noise should be incorporated in CSI-EPT. Initial studies show that filtering of the data allows us to handle measured data in foIC-EPT [20] and, as demonstrated in [14], total variation (TV) regularization may suppress noise effects in CSI-EPT. However, due to the many possible choices for the regularization parameter in this method, it is presently not clear for which parameter or parameter range the TV-CSI-EPT scheme is most effective.

Second, the phase that is measured in practice is not the phase of the B_1^+-field, but the so-called transceive phase from which the B_1^+-phase can be extracted. To this end, the transceive phase approximation is often applied, but the validity of this approximation is not fully understood and may lead to reconstruction errors in the conductivity and permittivity profiles [28]. Fortunately, it is shown in [31] that improved B_1^+-phase approximations can be obtained from the transceive phase by incorporating an iterative phase correction scheme in the CSI-EPT reconstruction algorithm. This correction scheme seems to reliably retrieve B_1^+-phase maps from the measured transceive phase and leads to improved conductivity and permittivity reconstructions compared with reconstructions that are obtained when the transceive phase approximation is applied. We will include this phase correction mechanism in future CSI-EPT implementations as well. Another option is to opt for phaseless approaches as, for example, proposed in [32, 33].

Finally, in practice the current densities in the transmit coil that generate the incident field depend on the object present, and we must account for this loading effect as well. Specifically, the integral representations for the fields in CSI-EPT are obtained using a scattered field formalism, in which it is assumed that the current density in the transmitting antenna is impressed and independent of the scatterer that may be present in the configuration. In practice, however, these currents do depend on the object and consequently care must be taken when we compute the background field in CSI-EPT. One approach is therefore to simulate this loading effect using a suitable coil and body model in a commercial field solver and to extract the current densities in the coil from this solver. The background field in CSI-EPT (the field without any load) can then computed using these extracted currents. In this way, the loading effect encountered in practice can be incorporated in our CSI-EPT reconstruction algorithm.

Our final aim is, of course, to turn CSI-EPT into a practical reconstruction method to obtain accurate and reliable conductivity and permittivity tissue maps of an interior part of the human body at MR frequencies of operation. Reconstruction results based on simulated data are very promising and we think that by addressing the practical is-

sues discussed above, we will indeed make significant progress towards a reliable EPT reconstruction method that provides us with accurate dielectric tissue maps in practice.

ACKNOWLEDGEMENT

The authors thank dr. Nico van den Berg of the Imaging Division of the University Medical Center Utrecht for many valuable discussions and support.

REFERENCES

[1] V. Hartwig, *Engineering for safety assurance in MRI: analytical, numerical and experimental dosimetry,* J. Magn. Reson. Imaging **33**, 681 (2015).

[2] J. Lagendijk, *Hyperthermia treatment planning,* Phys. Med. Biol. **45**, R61 (2000).

[3] U. Katscher and C. A. T. van den Berg, *Electric properties tomography: Biochemical, physical and technical background, evaluation and clinical applications,* NMR Biomed. **30**, e3729 (2017).

[4] S. Gabriel, R. Lau, and C. Gabriel, *The dielectric properties of biological tissues: Ii. measurements in the frequency range 10 hz to 20 ghz,* Phys. Med. Biol. **41**, 2251 (1996).

[5] B. H. Brown, *Electrical impedance tomography (EIT): a review,* J. Med. Eng. Technol. **27**, 97 (2003).

[6] R. Chandra, H. Zhou, I. Balasingham, and R. M. Narayanan, *On the opportunities and challenges in microwave medical sensing and imaging,* IEEE. Trans. Biomed. Eng. **62**, 1667 (2015).

[7] X. Zhang, J. Liu, and B. He, *Magnetic-resonance-based electrical properties tomography: a review,* IEEE Rev. Biomed. Eng. **7**, 87 (2014).

[8] G. Bal, *Hybrid inverse problems and internal functionals,* Inverse problems and applications: inside out. II **60**, 325 (2013).

[9] E. M. Haacke, L. S. Petropoulos, E. W. Nilges, and D. H. Wu, *Extraction of conductivity and permittivity using magnetic resonance imaging,* Phys. Med. Biol. **36**, 723 (1991).

[10] U. Katscher, T. Voigt, C. Findeklee, P. Vernickel, K. Nehrke, and O. Doessel, *Determination of electric conductivity and local SAR via B1 mapping,* IEEE Trans. Med. Imag. **28**, 1365 (2009).

[11] T. Voigt, U. Katscher, and O. Doessel, *Quantitative conductivity and permittivity imaging of the human brain using electric properties tomography,* Magn. Reson. Med. **66**, 456 (2011).

[12] A. L. van Lier, D. O. Brunner, K. P. Pruessmann, *et al.*, B_1^+ *phase mapping at 7 T and its application for in vivo electrical conductivity mapping,* Magn. Reson. Med. **67**, 552 (2012).

[13] F. S. Hafalir, O. F. Oran, N. Gurler, and Y. Z. Ider, *Convection-reaction equation based magnetic resonance electrical properties tomography (cr-MREPT),* IEEE Trans. Med. Imaging **33**, 777 (2014).

[14] E. Balidemaj, C. A. T. van den Berg, J. Trinks, *et al.*, *CSI-EPT: a contrast source inversion approach for improved MRI-based electric properties tomography,* IEEE Trans. Med. Imaging **34**, 1788 (2015).

[15] J. E. Serrallés, L. Daniel, J. K. White, D. K. Sodickson, R. Lattanzi, and A. G. Polimeridis, *Global Maxwell tomography: A novel technique for electrical properties mapping based on MR measurements and volume integral equation formulations,* in *2016 IEEE International Symposium on Antennas and Propagation (APSURSI)* (IEEE, 2016) pp. 1395–1396.

[16] R. Hong, S. Li, J. Zhang, *et al.*, *3-D MRI-based electrical properties tomography using the volume integral equation method,* IEEE Trans. Microw. Theory Tech. **65**, 4802 (2017).

[17] A. Arduino, L. Zilberti, M. Chiampi, and O. Bottauscio, *CSI-EPT in presence of RF-shield for MR-coils,* IEEE Trans. Med. Imag. **36**, 1396 (2017).

[18] A. Rahimov, A. Litman, and G. Ferrand, *MRI-based electric properties tomography with a quasi-newton approach,* Inverse Probl. **33**, 105004 (2017).

[19] N. Gurler and Y. Z. Ider, *Gradient-based electrical conductivity imaging using MR phase,* Magn. Reson. Med. **77**, 137 (2017).

[20] P. S. Fuchs, S. Mandija, P. R. Stijnman, W. M. Brink, C. A. van den Berg, and R. F. Remis, *First-order induced current density imaging and electrical properties tomography in MRI,* IEEE Trans. Comput. Imaging **4**, 624 (2018).

[21] P. M. van den Berg and A. Abubakar, *Contrast source inversion method: State of art,* Progress in Electromagnetics Research **34**, 189 (2001).

[22] P. M. van den Berg and R. E. Kleinman, *A contrast source inversion method,* Inverse Problems **13**, 1607 (1997).

[23] P. M. van den Berg, A. L. van Broekhoven, and A. Abubakar, *Extended contrast source inversion,* Inverse Probl. **15**, 1325 (1999).

[24] P. M. van den Berg and K. F. Haak, *Profile inversion by error reduction in the source type integral equations,* in *Wavefields and Reciprocity–Proceedings of a Symposium Held in Honour of Professor dr. AT de Hoop* (Citeseer, 1996) pp. 87–98.

[25] B. van den Bergen, C. C. Stolk, J. B. van den Berg, J. J. Lagendijk, and C. A. van den Berg, *Ultra fast electromagnetic field computations for RF multi-transmit techniques in high field MRI,* Phys. Med. Biol. **54**, 1253 (2009).

[26] R. L. Leijsen, W. M. Brink, C. A. van den Berg, A. G. Webb, and R. F. Remis, *3-D contrast source inversion-electrical properties tomography,* IEEE Trans. Med. Imaging **37**, 2080 (2018).

[27] A. Christ, W. Kainz, E. G. Hahn, *et al.*, *The virtual family – development of surface-based anatomical models of two adults and two children for dosimetric simulations,* Phys. Med. Biol. **55**, N23 (2009).

[28] A. L. H. M. W. van Lier, A. Raaijmakers, T. Voigt, *et al.*, *Electrical properties tomography in the human brain at 1.5, 3, and 7 T: a comparison study,* Magn. Reson. Med. **71**, 354 (2014).

[29] Y. Saad, *Iterative methods for sparse linear systems* (SIAM, 2003).

[30] E. Balidemaj, C. A. T. van den Berg, A. L. H. M. W. van Lier, *et al.*, *B_1-based SAR reconstruction using contrast source inversion-electric properties tomography (CSI-EPT),* Med. Biol. Eng. Comput. **55**, 225 (2017).

[31] P. R. S. Stijnman, S. Mandija, P. S. Fuchs, R. F. Remis, and C. A. T. van den Berg, *Transceive phase corrected contrast source inversion-electrical properties tomography,* in *Proc. 27th Annu. Meeting ISMRM* (2018) p. 5087.

[32] A. Arduino, O. Bottauscio, M. Chiampi, and L. Zilberti, *Magnetic resonance-based imaging of human electric properties with phaseless contrast source inversion,* Inverse Probl. **34**, 084002 (2018).

[33] M. T. Bevacqua, G. G. Bellizzi, L. Crocco, and T. Isernia, *A method for quantitative imaging of electrical properties of human tissues from only amplitude electromagnetic data,* Inverse Probl. **35**, 025006 (2019).